Acta Oceanol. Sin., 2021, Vol. 40, No. 1, P. 126–134
https://doi.org/10.1007/s13131-020-1675-0
http://www.hyxb.org.cn
E-mail: hyxbe@263.net

Dynamical features of near-inertial motions in global ocean based on the GDP dataset from 2000 to 2019

Manli Guo[1], Ruiyi Chen[1], Hongzhou Xu[2]*, Philip A Vetter[2]

[1] College of Oceanic and Atmospheric Sciences, Ocean University of China, Qingdao 266100, China

[2] Institute of Deep-sea Science and Engineering, Chinese Academy of Sciences, Sanya 572000, China

Received 4 July 2020; accepted 18 August 2020

Abstract

Based on the latest oceanic surface drifter dataset from the global drifter program during 2000–2019, this study investigated the global variation of relative frequency shift (RFS), near-inertial energy (NIE) and inverse excess bandwidth (IEB) of near-inertial motions, and analyzed their relations with oceanic mesoscale dynamics, relative vorticity and strain. Compared with previous works, we have some new findings in this study: (1) the RFS was high with negative values in some regions in which we found a significant blue shift of the RFS in the equatorward of 30°N (S) and from 50°N to 60°N in the Pacific, and a red shift in the western boundary currents and their extension regions, the North Atlantic and the Antarctic Circumpolar Current regions; (2) more peak values of the NIE were found in global regions like the South Indian Ocean, the Luzon Strait and some areas of the South Ocean; (3) the global distribution of the IEB were characterized by clear zonal bands and affected by vorticity and wind field; (4) the RFS was elevated as the absolute value of the gradient of vorticity increased, the IEB did not depend on the gradient of vorticity, and the eddy kinetic energy (EKE) weakened with the decrease of the absolute value of RFS; (5) the NIE decreased with increasing absolute value of the relative vorticity and the gradient of vorticity, but it increased with increasing strain and EKE when EKE was larger than 0.003 2 m^2/s^2.

Key words: near-inertial motions, frequency shift, decay timescale, surface drifter, mesoscale dynamics

Citation: Guo Manli, Chen Ruiyi, Xu Hongzhou, Vetter Philip A. 2021. Dynamical features of near-inertial motions in global ocean based on the GDP dataset from 2000 to 2019. Acta Oceanologica Sinica, 40(1): 126–134, doi: 10.1007/s13131-020-1675-0

1 Introduction

Near-inertial motions in the mixed layer, which are featured by clockwise (anticlockwise) rotation in the northern (southern) hemisphere with frequencies close to local inertial frequency *f*, contain half of the kinetic energy in the internal wave field in oceans (Ferrari and Wunsch, 2009). Surface wind is a dominant driver of the near-inertial motions in the mixed layer. The divergence/convergence caused by near-inertial motions can disturb the mixed layer and excite near-inertial internal waves that propagate downward and transfer energy from the mixed layer to the interior (Chen et al., 2017). It ultimately dissipates to micro-scale turbulent mixing by nonlinear wave-wave interactions (Alford et al., 2016). Therefore, the near-inertial motions are vitally important for multi-scale dynamic processes and energy budget in oceans.

In recent decades much attention has been paid to estimate the energy flux from wind to near-inertial motions. Alford (2001) estimated the distribution of the energy flux from wind to inertial motions in mixed layer from 50°S to 50°N by using NCEP-NCAR global reanalysis surface winds and a slab model. He concluded that the total power can reach 0.29 TW there, and 0.47 TW on the larger region of 70°S to 70°N (Alford, 2003). Watanabe and Hibiya (2002) estimated an energy flux of 0.7 TW on a similar global region except for a small difference in the South Ocean. Using a general circulation model, Simmons and Alford (2012) and Jochum et al. (2013) obtained the total wind-power input to near-inertial motions of 0.4 TW. Jiang et al. (2005) and Rimac et al. (2013) proved that different temporal and spatial resolutions of wind data would affect the magnitude or pattern of the energy flux. Due to the slab model's disadvantages that it does not consider dissipation mechanisms and it is sensitive to different wind products, observed drifter data was applied to calculated inertial energy in the mixing layer and the result can reach about 300 J/m^2 (Chaigneau et al., 2008). Liu et al. (2019) illustrated the global distribution of the mean near-inertial wind power using the wind stress based on computation without the ocean current imprint on wind stress and drifter data in which they gave a 0.31 TW of the global integrated power between 60°S to 60°N. In brief, these studies suggest that different methods of near-inertial energy estimation in the mixing layer give quantitatively different results.

The decay of near-inertial motion has been found by many researchers in different regions with timescale varying from 3 d to 5 d (Chen et al., 2013; Kim et al., 2014; Park et al., 2009). Using a numerical model, Park et al. (2009) presented a global map of decay timescale of near-inertial motion in which they suggested that the timescale increased with higher latitude. Using drifter data during 2000–2007, Elipot et al. (2010) estimated the global

Foundation item: The Global Change and Air-Sea Interaction Project under contract No. GASI-IPOVAI-01-03; the National Key Research and Development Program under contract Nos 2016YFC1401403 and 2018YFC0309800; the National Natural Science Foundation of China under contract Nos 41576009 and 41576006; the Strategic Priority Research Program of the CAS under contract No. XDA13030302; the Chinese Academy of Sciences Frontier Basic Research Project under contract No. QYJC201910.
*Corresponding author, E-mail: hzxu@idsse.ac.cn

near-inertial energy, the decay timescale, and the frequency shift of near-inertial motions. However, the complete and precise global distributions of the three variables were not attainable from the limited number of drifters available then. During the last two decades, a large number of drifters have been deployed to collect global oceanic data that enable us to explore them more extensively and precisely.

In this study, we used the latest drifter dataset to investigate the global pattern of near-inertial motion features including relative frequency shift (RFS), inverse excess bandwidth (IEB) and near-inertial energy (NIE) in the mixed layer, which represented the refraction, decay timescale and energy of near-inertial motions, respectively. Furthermore, their relations with mesoscale dynamics, vorticity and strain were discussed. This paper is organized as follows. Section 2 introduces the data and methods. Section 3 gives the global map of near-inertial motions and their seasonal cycles. Section 4 discusses the relationship between near-inertial motions and mesoscale dynamics. Section 5 summarizes the paper.

2 Data and methods

2.1 *Data*

The Global Drifter Program (GDP) dataset from 2000 to 2019 was used to investigate the features of the near-inertial motions in this study (https://www.aoml.noaa.gov/phod/gdp/hourly_data.php). The drifter records were sampled at 15 m depth. The velocity fields were derived from the locations of the drifters which were sampled temporally and randomly with the time interval of 1–2 h. In this paper, we utilized the interpolation product of regular 1-h time series (Elipot and Lumpkin, 2008). We excluded datapoints ranging between 10°N–10°S for avoidance of problems with geostrophic effect (Elipot et al., 2010). The number of drifter velocity observations were counted in each 1°×1° bin (Fig. 1). The total number of datapoints reached about 1.24×10^8. The product density was much higher and the domain was much larger than in previous studies (Elipot et al., 2010).

To explore the relationship between the near-inertial motions and the mesoscale dynamics, we used sea level anomaly (SLA) dataset to calculate the relative vorticity, gradient of the relative vorticity, eddy kinetic energy (EKE). We used strain downloaded from the AVISO product with resolutions of 0.25°×0.25° in spatial and 1 d in temporal (https://www.aviso.altimetry.fr/home.html). In addition, the Argo profiles product was applied to estimate the global climatological mixed layer depth and the near-inertial kinetic energy (Holte et al., 2017). To match the drifter dataset, all above quantities were interpolated into the same resolution in space and time.

2.2 *Methods*

The drifter trajectories were separated into 2.5×10^5 segments every 20 d without overlapping and each segment contained 480 observations as an independent unit (Elipot et al., 2016). Using the quadratic multitaper method with 6 tapers for a time bandwidth product of 4 (Prieto et al., 2007), the velocity frequency spectra were computed for all the segments. The diurnal and semidiurnal tidal signals could be incorrect for the near-inertial peaks at the area near latitude 30° and 75°, so tidal-induced barotropic velocity was subtracted from each velocity segment before the spectral analysis at these areas. The barotropic velocities were derived from the Oregon State University Topex/Poseidon global inverse solution (Egbert and Erofeeva, 2002). Due to insufficient data the baroclinic components of tides were not subtracted.

The RFS was defined as

$$\mathrm{RFS} = \frac{\omega_\mathrm{p} - f}{f},$$

where f was the inertial frequency of the mean latitude of the corresponding 20-d trajectory, ω_p was the spectral peak frequency which was closest to f. If ω_p–f was higher than $0.2f$, or the spectral peak of ω_p was less than decuple the background spectral magnitude, this RFS was discarded. A positive (negative) RFS means that the frequency of the motion was higher than f, namely blue (red) shift.

The inverse excess bandwidth (IEB) was defined as

$$\mathrm{IEB} = \frac{1}{\Delta\omega - \Delta\omega_\mathrm{r}},$$

where the bandwidth $\Delta\omega$ was defined as the difference between the frequencies where the power falls to one half of peak value ω_p. The minimum bandwidth $\Delta\omega_\mathrm{r}$ was the time bandwidth product (which was 4 in our study) times the spectral resolution.

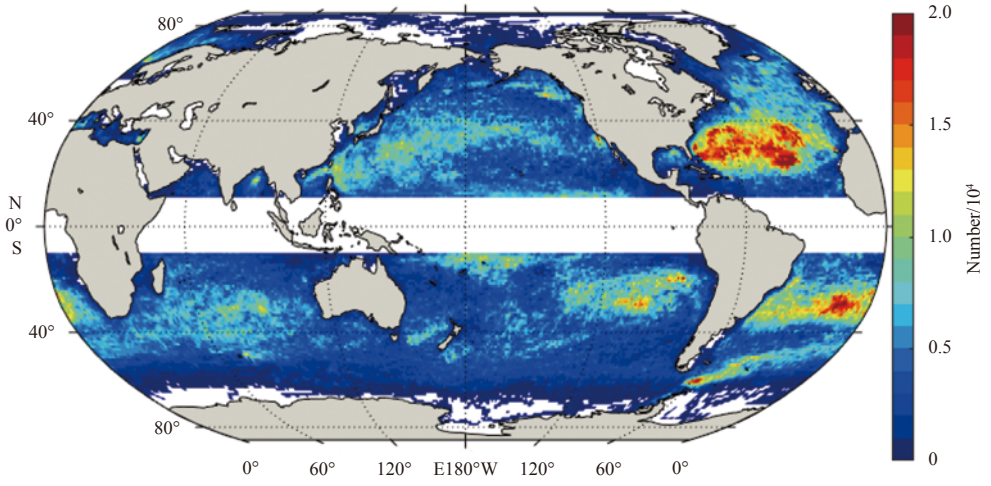

Fig. 1. The number of velocity observations in 1°×1° bins.

The IEB represented the decay timescale of the NIO, and the relationship of IEB and decay timescale were shown in Fig. 3 in the work by Elipot et al. (2010).

Assuming that the near-inertial velocity was vertically uniform over the mixed layer depth, the NIE was calculated as

$$\mathrm{NIE} = \frac{1}{2}\rho u_{\mathrm{NI}}^2 H_{\mathrm{mix}}. \quad (1)$$

The u_{NI}^2 was estimated by near-inertial variance (NIV) of the near-inertial motions. $u_{\mathrm{NI}}^2 = \mathrm{NIV} = \int_{\Delta\omega} S(\omega)\,\mathrm{d}\omega$, where $S(\omega)$ was the velocity frequency spectra for each segment, ρ was the density (ρ=1 025 g/m^3), and H_{mix} was mixed layer depth. After that, the RFS, NIE and IEB were averaged in each spatial bin and every hour in temporal weighting by the length of time that a drifter spent in each bin.

3 Results

3.1 *The global distribution of the RFS, NIE and IEB*

3.1.1 *The RFS*

Figure 2 shows that the RFS varied geographically with a mean value of 0.012 6 interlaced with blue and red shifts. It can be seen that the blue shift of the RFS predominated from 30°N to 30°S, 55° N to 70°N and in the Drake Passage. The red shift of the RFS dominated the areas of the western boundary currents, their extension (the Kuroshio and Gulf Stream), and the Agulhas Retroflection. In the mid-latitude band (30°–55°) of the Pacific basin and the Southern Ocean, the RFS was relatively small and usually positive (blue shift).

The propagation of near-inertial motions can cause the difference between their intrinsic frequency and local Coriolis frequency because of the β effect and lead to blue shift of near-inertial motions (Fu, 1981; Garrett, 2001). The blue shift between 30°N and 30°S also were found by Elipot et al. (2010) where the near-inertial motions were intensively generated by the storm (Chang et al., 2002; Alford et al., 2016) and propagated long distances toward the equator, resulting in a significant large RFS. Moreover, there was the possibility that the blue shift near 75° and 30° may be associated with the internal tide, since the inertial frequency is close to the frequency of diurnal and semi-diurnal tide at these places, such as the strong blue shift in the Drake Passage (Li et al., 2015). Even so, the blue shift near 70°N was more likely to be caused by the near-inertial motions rather than the internal tide because the strength of RFS has an obvious seasonal cycle (see Section 3.2).

In addition, the vorticity of the background field (ζ) can shift the local inertial frequency by $\zeta/2$ and further lead to red shift of the RFS (Kunze, 1985; Whale et al., 2018; Zhang et al., 2018). Figure 2a shows that the red shift occurred at regions with active eddies that was consistent with the background vorticity field (Fig. 2c). Jeon et al. (2019) stated that poleward propagation of near-inertial motions was generated at western boundary current, since the inertial frequency at low latitude was lower than it at high latitude. This propagation could further lead to the red shift. Therefore, the red shift in the western boundary current region could be motivated by both eddy and strong current. Noted that the portion of negative RFS at the 30°–55°N latitude of the Atlantic was larger than that of the Pacific except for in the western boundary currents and their extension regions. The mechanism of this asymmetry between the two basins is still unclear.

3.1.2 *The NIE*

Since the NIV excluded the mixed layer, to understand the global energy budget at the upper oceans, we calculated the NIE in global scale (Fig. 3a). It can be seen that our results were comparable with previous results derived from the slab model (Alford, 2001; Alford, 2003; Watanabe and Hibiya, 2002) and drifter data (Liu et al., 2019). The peak values of the NIE with about 800 J/m^2 occurred at the high latitudes of the North Pacific and the South Indian Ocean coinciding with the location of storm

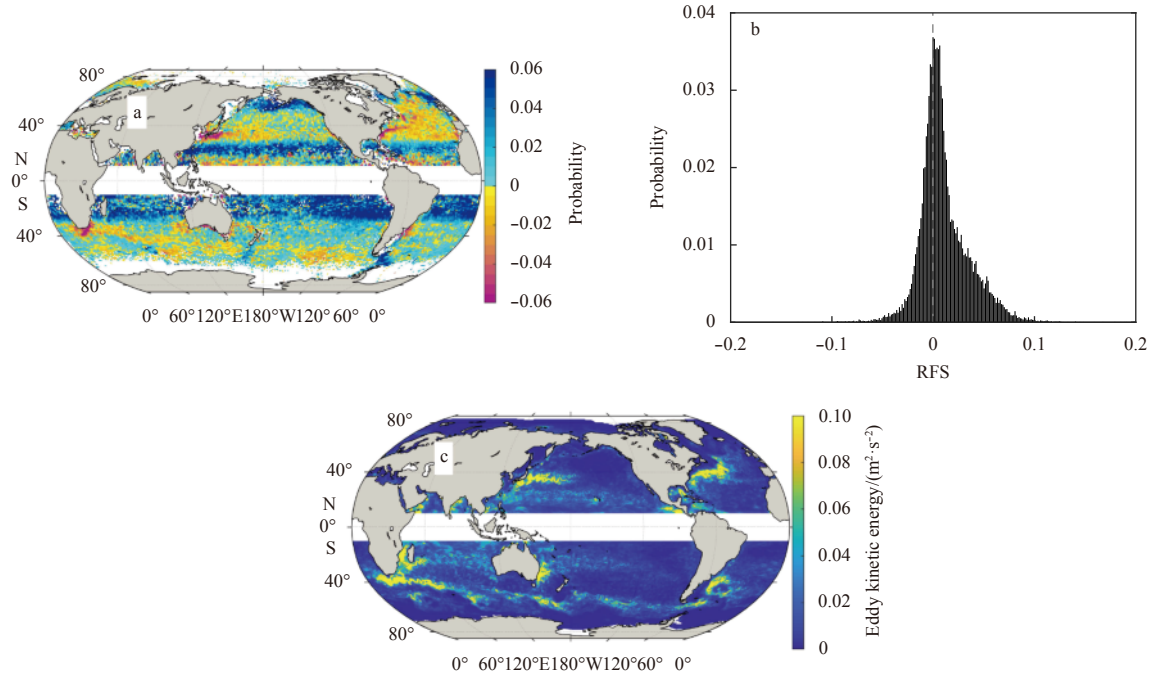

Fig. 2. The global (a) and probability (b) distributions of RFS, and the global distribution of temporal average eddy kinetic energy (c).

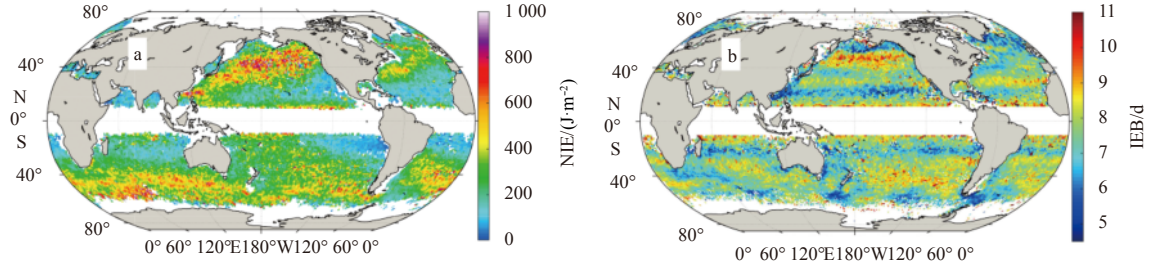

Fig. 3. The averaged NIE (a) and IEB (b) in 1°×1° bins.

tracks (Chang et al., 2002). In addition, the peak values of the NIE also appeared at the Luzon Strait, where immense energy of internal wave were found (Hsu and Liu, 2000). In the North Atlantic and the rest areas of the South Ocean, the NIE were still strong with values of about 500 J/m^2. Overall, the averaged global value of the NIE reached about 300 J/m^2, consistent with Chaigneau et al. (2008).

3.1.3 *The IEB*

Figure 3b shows the global distribution of the IEB characterized by clear zonal bands, which was excluded in Elipot et al. (2010) for lack of data. The modal value of the IEB was 7.5 d, corresponding to an exponential decay timescale of approximately 2 d based on the conversion relation between the two variables (Elipot et al., 2010), which was half of the common decay timescale (Park et al., 2009). In the North Pacific, the values of the IEB were relatively low in the 15°–20°N and 50°–60°N latitude band. But they were relatively high from 40° to 50°N corresponding to the region with high NIE in Fig. 3a because near-inertial motions with higher energy could take more time to decay. There were low values from 50° to 60°N in the North Atlantic, and a narrow band of high values near 30°N. The results suggested that the decay timescale in the North Atlantic was unlike the North Pacific having such a trend of increase with latitude (Park et al., 2009). In the southern hemisphere, low values occurred in the 15°–20°S latitude band, which was similar with the North Pacific. Moreover, low values also were found at the region with high EKE in Fig. 2c, perhaps owing to the rectification effect of the relative vorticity (Park et al., 2009). Differ to Park et al. (2009), we can see that high values of the IEB occur near 30° in the northern hemisphere overlapping the area where the frequency of internal tide equals to f in this study, and this coincidence should be discussed further in future.

3.1.4 *The relations of the RFS, NIE and IEB*

To understand the relations among the three variables, we compared them pairwise (Fig. 4). The x-coordinate was divided into several bins and the average values of the parameters belonging to each bin were computed. In Figs 4a and b, we chose the RFS as the x-coordinate to avoid average RFS values. It can be seen that both the NIE and IEB reached their peak values when the IEB was close to zero, while they reduced gradually with increase of the absolute RFS. Moreover, the NIE was almost proportional to the IEB with small fluctuations (Fig. 4c).

3.2 *The seasonal cycle of the RFS, NIE and IEB*

We averaged the all three parameters during each season and plot them in Fig. 5. A significant seasonal variation of these variables is evident, suggesting the important role of the wind field on modulating the near-inertial motions. They all showed maximum values in winter, and gradually reduced from autumn, summer to spring. In specific, the mean value of the RFS in winter was about 0.13, which was 3.9 times higher than it in spring. Although the magnitudes of the RFS varied with time, spatial structures persisted (Fig 5a). Note that the magnitude of the RFS from 30° to 60°S reached the maximum in autumn rather than in winter.

The NIE reached a mean value of about 1 290 J/m^2 in winter, 4.3 times larger than in spring (Fig. 5b). Its seasonal variability was much more significant than found by previous studies (Chaigneau et al. 2008; Liu et al., 2019). The seasonal variations of the NIE were weaker in the southern hemisphere than in the northern, consistent with the global distribution of wind field (Chang et al., 2002). The magnitudes of the IEB varied largely with different seasons as well (Fig 5c). The 30-d running average was 4 times higher in winter than in spring. The IEB showed large values near 30°N in summer and autumn, but it disappeared in winter and spring.

4 Correlation analysis

It was found that geostrophic vorticity can accelerate the decay of mixed-layer near-inertial motions (D'Asaro, 1995).

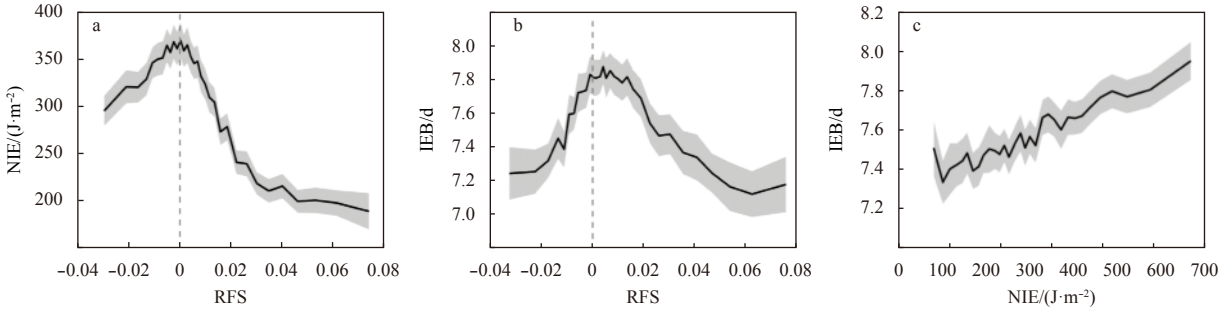

Fig. 4. The relations between the NIE and RFS (a), the IEB and RFS (b), and the NIE and IEB (c). The gray shading represented one-tenth of the standard error of the mean value for each bin.

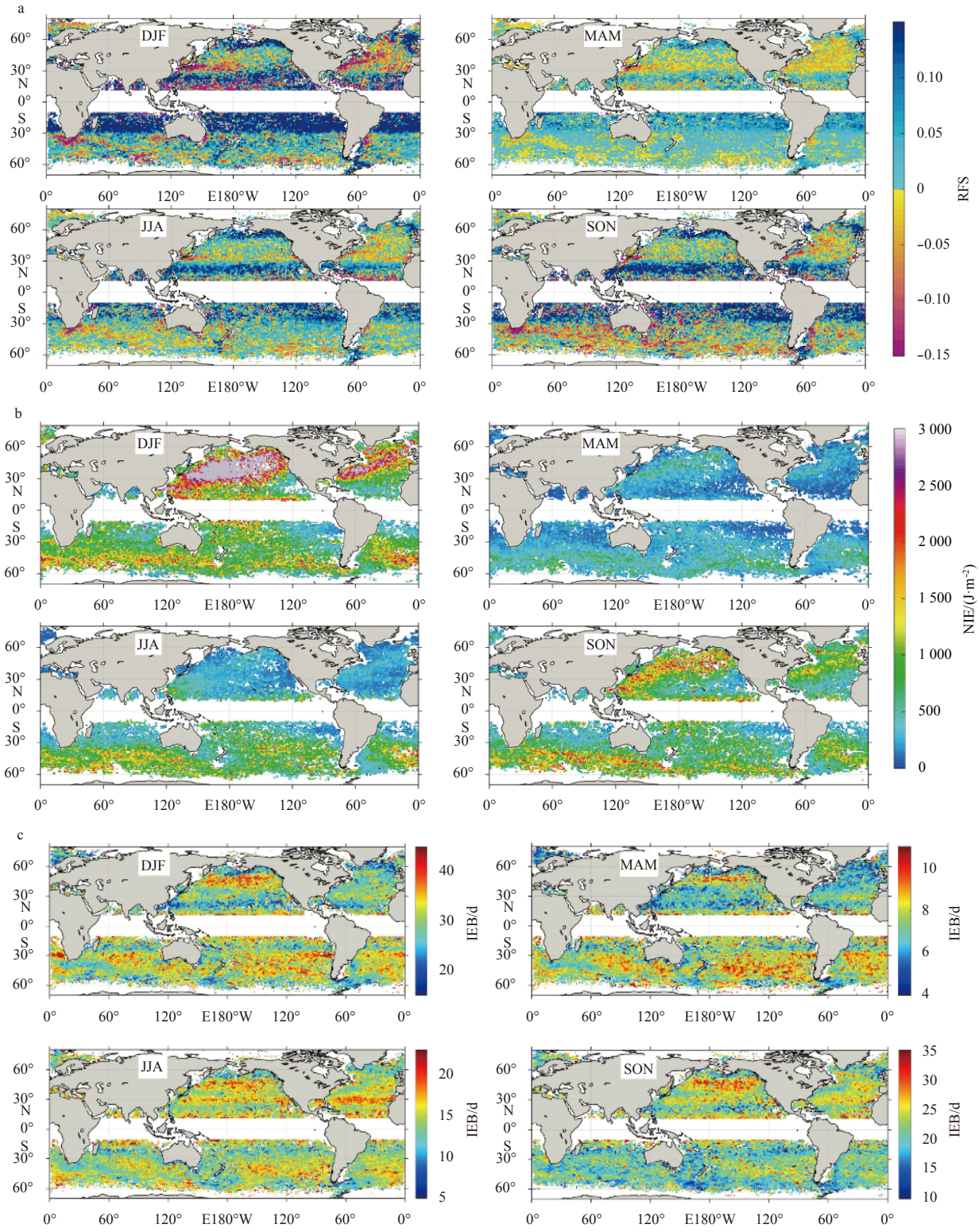

Fig. 5. Global distribution of the averaged RFS (a), NIE (b) and IEB (c) during winter (DJF), spring (MAM), summer (JJA) and autumn (SON) in 1°×1° bins.

Moreover, van Meurs (1998) claimed that the gradients of the mesoscale vorticity would affect the generation and evolution of near-inertial currents in the mixed layer. According to Polzin (2008) and Polzin (2010), the mesoscale strain field affected both energy and wavenumber of near-inertial waves. To explore the influence of different mesoscale dynamics on the near-inertial motions further, we examined the relations between the parameters of near-inertial motions and the relative vorticity, gradient of relative vorticity, EKE and strain in this section.

4.1 *Vorticity*

As shown in Fig. 6a, the RFS was proportional to the relative

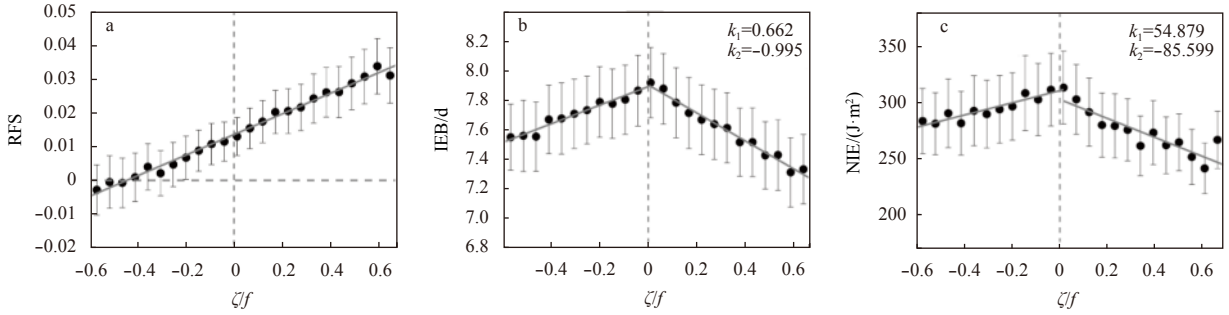

Fig. 6. The RFS (a), IEB (b), NIE (c) binned with the values of ζ/f. The gray line in each plot indicates the fitted lines of the dots. k_1 and k_2 in panel b and c is the slope of the gray lines.

vorticity (ζ/f), and the slope of the fitted line was about 0.03, which was relative smaller than 0.39 given by Elipot et al. (2010), who suggested that this value was consistent with the theory of Kunze (1985). This discrepancy occurred because the scales of eddies must be larger than the scale of near-inertial motions in the theory of Kunze (1985), which was not real in the ocean (Young and Ben Jelloul, 1997). The intercept of the fitted line was 0.014, larger than 0.007 in Elipot et al. (2010), indicating that the β effect was of great importance in our study.

The IEB declined with the increase of the absolute value of the relative vorticity (Fig. 6b). And it has faster declining rate for cyclone vorticity, which might be caused by the opposite direction to the rotation between the cyclone vorticity and the near-inertial motions. The NIE similarly declined with the increasing absolute value of the relative vorticity (Fig. 6c). But it showed spatial variation in different regions. Its trend between 30°N and 30°S was inverse compared with global trend of the NIE where the NIE decreased to the minimum value when the relative vorticity was zero. While it kept the same trend with global pattern from 30° to 60°N (S) (not shown).

4.2 *Gradient of vorticity*

In this study, we used the multiplication of magnitude of the gradient of relative vorticity and the sign of ζ/f to represent the gradient of vorticity, so that the positive (negative) values indicated cyclone (anticyclone) eddies. Although larger gradient of vorticity corresponded to larger vorticity (not shown), the relation between the RFS and the relative vorticity gradient was different with that between the RFS and the relative vorticity (Figs 6a and 7a). It can be seen that the RFS raised with the increase of the absolute value of the gradient of relative vorticity both for the cyclone and anticyclone eddies, which was different with the results by Elipot et al. (2010). On the contrary, the NIE declined with the increase of the absolute value of the gradient of relative vorticity (Fig. 7c). This was consistent with the theory claimed by van Meurs (1998) in which he found that the mesoscale caused the frequency shift and the wavenumber shift to increase for higher modes and larger gradient of vorticity would lead to a faster separation of higher modes near-inertial motions resulting in a faster decay of near-inertial energy in the mixed layer. However, the IEB was independent on the gradient of relative vorticity (Fig. 7b).

4.3 *Eddy kinetic energy and strain*

In this section, the dependence of the NIE and IEB on EKE and strain were discussed (Fig. 8). Here the strain was defined as $\sqrt{S_n^2+S_s^2}$, where $S_s=\partial v/\partial x+\partial u/\partial y$ was the shear component of strain, and $S_n=\partial u/\partial x-\partial v/\partial y$ was the normal component. Figure 8a shows that the NIE reduced almost linearly with the increase of $\log_{10}$(EKE) when EKE was less than the threshold of 0.003 2 m^2/s^2. Above this threshold, the NIE has the positive linear relation with the $\log_{10}$(EKE) by and large. The similar trend can be found between the NIE and the strain (Fig. 8b). This relation conformed to the conclusion from Jing et al. (2017) that the strain was responsible for the energy transferring from geostrophic flow to near-inertial motions. Contrary to the NIE, the IEB decreased almost linearly as the $\log_{10}$(EKE) and strain rose after the threshold, indicating that both the eddies and strain would accelerate the decay of near-inertial motions (Figs 8c and d).

In addition, the relations between the RFS and EKE, strain were examined as well in this section, and the RFS was chosen as x-coordinate to avoid averaged RFS condition (Fig. 9). Figure 9a reveals that EKE declined as the decrease of the absolute RFS but with different decline rate on either side of zero of the RFS. The EKE were reduced faster when the RFS was negative indicating

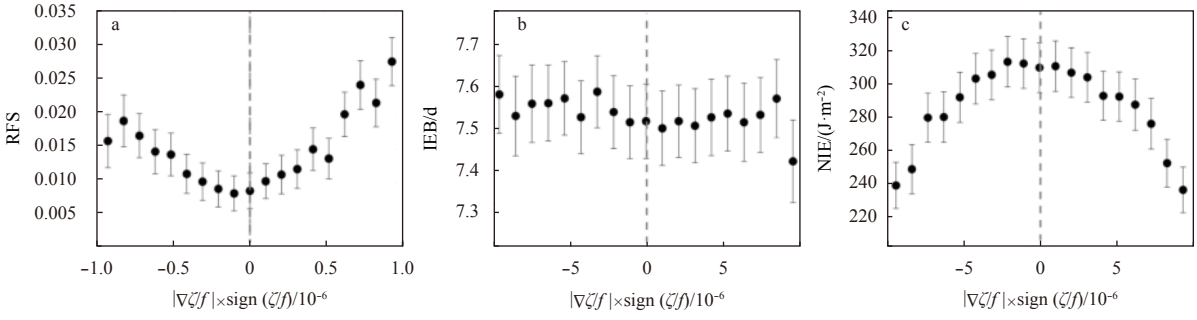

Fig. 7. RFS (a), IEB (b), NIE (c) binned with values of $|\nabla\zeta/f|\times\text{sign}(\zeta/f)$.

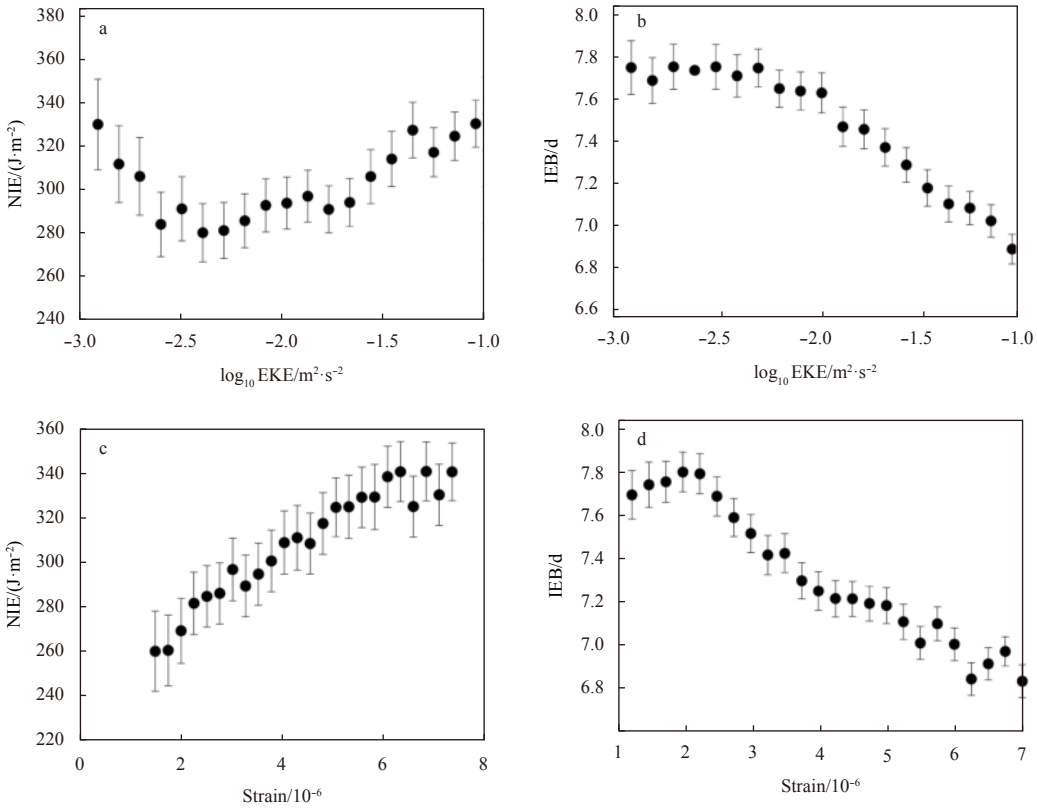

Fig. 8. NIE (a), IEB (b) binned by values of EKE; NIE(c), IEB (d) binned by values of strain.

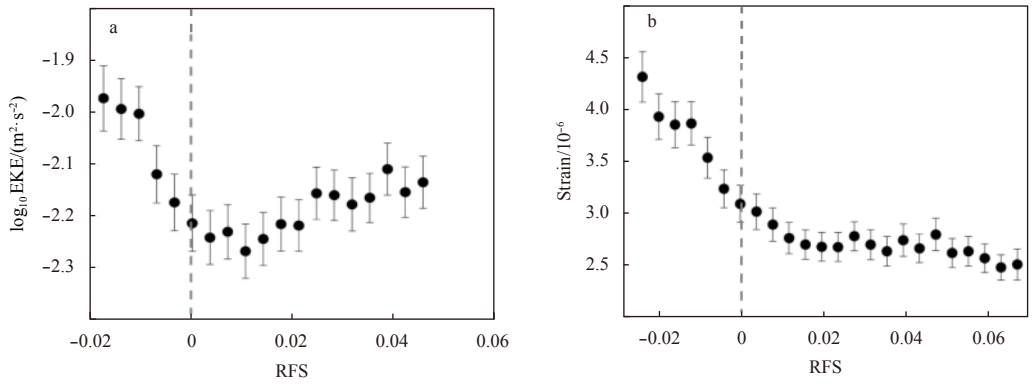

Fig. 9. EKE (a), strain (b) binned by values of RFS, with RFS being *x*-coordinate to avoid average RFS values.

the different decreasing rate may be associated with the amplitude of anticyclone being higher than cyclone at the surface (Chelton et al., 2011; Cheng et al., 2014). And the strain and RFS kept negative relation in overall.

5 Summary

By using the latest GDP drifter and satellite SLA datasets, we investigated the features of global near-inertial motions, including RFS, NIE and IEB and analyzed the influence of mesoscale vorticity and strain on these variables. We found that the red shift occurred at the regions with active mesoscale eddy and anticyclone eddy exerted more influence on the frequency shift of near-inertial motions than cyclone eddy. The pattern of NIE was mainly modulated by the energy flux from the wind to near-inertial motions. The distribution of IEB was characterized by a zonal band in Which it reached the maximum value at the mid-latitude of the North Pacific corresponding to the region of largest NIE. In seasonal mean, the variation of three variables showed significant seasonal cycle in which the magnitude of RFS, IEB and NIE rose in the winter and declined in the spring. This trend was consistent with the variability of the wind field, suggesting that wind was crucial for modulating the near-inertial motions.

The relations between vorticity, gradient of the vorticity, EKE, strain and the three variable showed diversity in this study. The slope of the fitted line of ζ/f and RFS was very different from the theory of Kunze (1985). The intercept was twice that in Elipot et al. (2010), implying the β effect may be a key factor on affecting RFS in global scale. The IEB was independent of the gradient of vorticity. The RFS increased as the absolute value of the gradient of vorticity rose. Moreover, the NIE increased with EKE and

strain, suggesting that the strain may be responsible for the energy transferring from geostrophic flow to near-inertial motions (Jing et al., 2017). We assumed that our results perhaps contained the signals of internal tide which could lead to some inaccuracy inevitably. In future, more field experiments and exploration are expected.

Acknowledgements

We thank the GDP Data Assembly Center for providing the quality-controlled data set. The mixed layer depth data are available at http://mixedlayer.ucsd.edu/.

References

Alford M H. 2001. Internal swell generation: The spatial distribution of energy flux from the wind to mixed layer near-inertial motions. Journal of Physical Oceanography, 31(8): 2359–2368, doi: 10.1175/1520-0485(2001)031<2359:ISGTSD>2.0.CO;2

Alford M H. 2003. Improved global maps and 54-year history of wind-work on ocean inertial motions. Geophysical Research Letters, 30(8): 1424, doi: 10.1029/2002GL016614

Alford M H, MacKinnon J A, Simmons H L, et al. 2016. near-inertial internal gravity waves in the ocean. Annual Review of Marine Science, 8: 95–123, doi: 10.1146/annurev-marine-010814-015746

Chaigneau A, Pizarro O, Rojas W. 2008. Global climatology of near-inertial current characteristics from Lagrangian observations. Geophysical Research Letters, 35(13): L13603, doi: 10.1029/2008GL034060

Chang E K M, Lee S, Swanson K L. 2002. Storm track dynamics. Journal of Climate, 15(16): 2163–2183, doi: 10.1175/1520-0442(2002)015<02163:STD>2.0.CO;2

Chelton D B, Schlax M G, Samelson R M. 2011. Global observations of nonlinear mesoscale eddies. Progress in Oceanography, 91(2): 167–216, doi: 10.1016/j.pocean.2011.01.002

Chen Shengli, Chen Daoyi, Xing Jiuxing. 2017. A study on some basic features of inertial oscillations and near-inertial internal waves. Ocean Science, 13(5): 829–836, doi: 10.5194/os-13-829-2017

Chen Gengxin, Xue Huijie, Wang Dongxiao, et al. 2013. Observed near-inertial kinetic energy in the northwestern South China Sea. Journal of Geophysical Research: Oceans, 118(10): 4965–4977, doi: 10.1002/jgrc.20371

Cheng Y H, Ho C R, Zheng Quanan, et al. 2014. Statistical characteristics of mesoscale eddies in the north pacific derived from satellite altimetry. Remote Sensing, 6(6): 5164–5183, doi: 10.3390/rs6065164

D'Asaro E A. 1995. Upper-ocean inertial currents forced by a strong storm. Part III: Interaction of inertial currents and mesoscale eddies. Journal of Physical Oceanography, 25(11): 2953–2958, doi: 10.1175/1520-0485(1995)025<2953:UOICFB>2.0.CO;2

Egbert G D, Erofeeva S Y. 2002. Efficient inverse modeling of barotropic ocean tides. Journal of Atmospheric and Oceanic Technology, 19(2): 183–204, doi: 10.1175/1520-0426(2002)019<0183:EIMOBO>2.0.CO;2

Elipot S, Lumpkin R. 2008. Spectral description of oceanic near-surface variability. Geophysical Research Letters, 35(5): L05606

Elipot S, Lumpkin R, Perez R C, et al. 2016. A global surface drifter data set at hourly resolution. Journal of Geophysical Research: Oceans, 121(5): 2937–2966, doi: 10.1002/2016JC011716

Elipot S, Lumpkin R, Prieto G. 2010. Modification of inertial oscillations by the mesoscale eddy field. Journal of Geophysical Research: Oceans, 115(9): C09010

Ferrari R, Wunsch C. 2009. Ocean circulation kinetic energy: Reservoirs, sources, and sinks. Annual Review of Fluid Mechanics, 41: 253–282, doi: 10.1146/annurev.fluid.40.111406.102139

Fu L L. 1981. Observations and models of inertial waves in the deep ocean. Reviews of Geophysics, 19(1): 141–170, doi: 10.1029/RG019i001p00141

Garrett C. 2001. What is the "near-inertial" band and why is it different from the rest of the internal wave spectrum?. Journal of Physical Oceanography, 31(4): 962–971, doi: 10.1175/1520-0485(2001)031<0962:WITNIB>2.0.CO;2

Holte J, Talley L D, Gilson J, et al. 2017. An Argo mixed layer climatology and database. Geophysical Research Letters, 44(11): 5618–5626, doi: 10.1002/2017GL073426

Hsu M K, Liu A K. 2000. Nonlinear internal waves in the South China Sea. Canadian Journal of Remote Sensing, 26(2): 72–81, doi: 10.1080/07038992.2000.10874757

Jeon C, Park J H, Nakamura H, et al. 2019. Poleward-propagating near-inertial waves enabled by the western boundary current. Scientific Reports, 9: 9955, doi: 10.1038/s41598-019-46364-9

Jiang Jing, Lu Youyu, Perrie W. 2005. Estimating the energy flux from the wind to ocean inertial motions: The sensitivity to surface wind fields. Geophysical Research Letters, 32(15): L15610, doi: 10.1029/2005GL023289

Jing Zhao, Wu Lixin, Ma Xiaohui. 2017. Energy exchange between the mesoscale oceanic eddies and wind-forced near-inertial oscillations. Journal of Physical Oceanography, 47(3): 721–733, doi: 10.1175/JPO-D-16-0214.1

Jochum M, Briegleb B, Danabasoglu G, et al. 2013. The impact of oceanic near-inertial waves on climate. Journal of Climate, 26(9): 2833–2844, doi: 10.1175/JCLI-D-12-00181.1

Kim S Y, Kosro P M, Kurapov A L. 2014. Evaluation of directly wind-coherent near-inertial surface currents off Oregon using a statistical parameterization and analytical and numerical models. Journal of Geophysical Research: Oceans, 119(10): 6631–6654, doi: 10.1002/2014JC010115

Kunze E. 1985. Near-inertial wave propagation in geostrophic shear. Journal of Physical Oceanography, 15(5): 544–565, doi: 10.1175/1520-0485(1985)015<0544:NIWPIG>2.0.CO;2

Li Zhuhua, Von Storch J S, Müller M. 2015. The M_2 internal tide simulated by a 1/10° OGCM. Journal of Physical Oceanography, 45(12): 3119–3135, doi: 10.1175/JPO-D-14-0228.1

Liu Yongzheng, Jing Zhao, Wu Lixin. 2019. Wind power on oceanic near-inertial oscillations in the global ocean estimated from surface drifters. Geophysical Research Letters, 46(5): 2647–2653, doi: 10.1029/2018GL081712

Park J J, Kim K, Schmitt R W. 2009. Global distribution of the decay timescale of mixed layer inertial motions observed by satellite-tracked drifters. Journal of Geophysical Research: Oceans, 114(11): C11010

Polzin K L. 2008. Mesoscale eddy-internal wave coupling. Part I: Symmetry, wave capture, and results from the mid-ocean dynamics experiment. Journal of Physical Oceanography, 38(11): 2556–2574, doi: 10.1175/2008JPO3666.1

Polzin K L. 2010. Mesoscale eddy-internal wave coupling. part II: energetics and results from PolyMode. Journal of Physical Oceanography, 40(4): 789–801, doi: 10.1175/2009JPO4039.1

Prieto G A, Parker R L, Thomson D J, et al. 2007. Reducing the bias of multitaper spectrum estimates. Geophysical Journal International, 171(3): 1269–1281, doi: 10.1111/j.1365-246X.2007.03592.x

Rimac A, Von Storch J S, Eden C, et al. 2013. The influence of high-resolution wind stress field on the power input to near-inertial motions in the ocean. Geophysical Research Letters, 40(18): 4882–4886, doi: 10.1002/grl.50929

Simmons H L, Alford M H. 2012. Simulating the long-range swell of internal waves generated by ocean storms. Oceanography, 25(2): 30–41, doi: 10.5670/oceanog.2012.39

van Meurs P. 1998. Interactions between near-inertial mixed layer currents and the mesoscale: The importance of spatial variabilities in the vorticity field. Journal of Physical Oceanography, 28(7): 1363–1388, doi: 10.1175/1520-0485(1998)028<1363:IBNIML>2.0.CO;2

Watanabe M, Hibiya T. 2002. Global estimates of the wind-induced energy flux to inertial motions in the surface mixed layer. Geo-

physical Research Letters, 29(8): 1239

Whalen C B, MacKinnon J A, Talley L D. 2018. Large-scale impacts of the mesoscale environment on mixing from wind-driven internal waves. Nature Geoscience, 11(11): 842–847, doi: 10.1038/s41561-018-0213-6

Young W R, Jelloul M B. 1997. Propagation of near-inertial oscillations through a geostrophic flow. Journal of Marine Research, 55(4): 735–766, doi: 10.1357/0022240973224283

Zhang Zhiwei, Qiu Bo, Tian Jiwei, et al. 2018. Latitude-dependent finescale turbulent shear generations in the Pacific tropical-extratropical upper ocean. Nature Communications, 9: 4086, doi: 10.1038/s41467-018-06260-8